

1 **Manuscript submitted to "Colloids and Surfaces A: Physicochemical and Engineering**
2 *Aspects*" as a research paper.

3

4

5 Synergistic piezophototronic and plasmonic effects in Pt-Pd/BiVO₄ composites for
6 enhanced tetracycline degradation

7

8

9

10 Hao Sun^a, Xu Zhao^{a*}, Martin R. Tillotson^b, Wei Guo^{c*}

11 ^a*Institute of Blue and Green Development, Shandong University, 264209 Weihai, China*

12 ^b*School of Civil Engineering, University of Leeds, Leeds LS2 9JT, United Kingdom*

13 ^c*College of Architecture and Civil Engineering, Beijing University of Technology, Beijing,*

14 *China*

15

16

17

18 *Corresponding author.

19 *E-mail addresses:* xuzhao@sdu.edu.cn; gwfjybj@bjut.edu.cn

20 **Abstract**

21 Piezo-photocatalysis has emerged as a promising strategy for environmental
22 remediation, particularly in addressing persistent organic pollutants such as antibiotics.
23 However, its practical implementation faces two critical challenges: (1) rapid recombination
24 of photogenerated electron-hole pairs and (2) insufficient active sites for surface redox
25 reactions. To overcome these limitations, we developed an innovative piezo-photocatalytic
26 system composed of ultrathin BiVO₄ nanosheets decorated with bimetallic Pt-Pd alloy
27 nanoparticles (Pt-Pd/BiVO₄) for efficient tetracycline (TC) degradation. As an efficient
28 combination of photocatalysis and piezocatalysis, the built-in polarization field generated by
29 the piezoelectric effect of BiVO₄ catalysts could serve as a powerful driving force for the
30 separation and migration of photoexcited charges. Simultaneously, the Pt-Pd nanoparticles
31 enhance catalytic performance through (i) localized surface plasmon resonance (LSPR)-
32 induced hot electron generation and (ii) optimized charge transfer pathways due to their
33 superior electrical conductivity. Under simultaneous ultrasonic vibration and visible light
34 illumination, the PPB-0.5 composites achieves an outstanding TC degradation rate constant
35 ($k = 0.071 \text{ min}^{-1}$), representing a 3.54-fold enhancement compared to pure BiVO₄.
36 Furthermore, the degradation efficiency remains nearly 90% after four cycles, highlighting
37 the system's stability. The result reveal that the synergistic coupling of photocatalysis,
38 piezoelectric polarization and plasmonic excitation significantly promotes the generation of
39 reactive oxygen species (ROS), particularly $\cdot\text{OH}$ and $\cdot\text{O}_2^-$ radicals, which play a dominant
40 role in TC degradation. This work not only provides fundamental insights into piezo-photo-
41 plasmonic coupling effects but also offers a viable design strategy for developing robust
42 hybrid catalysts for wastewater treatment applications.

43 Keywords: Pt-Pd bimetallic nanoparticle; BiVO₄; Piezo-photocatalysis; Synergistic effect;

44 Tetracycline degradation

45

46 **1. Introduction**

47 Over the past few decades, antibiotics have been widely utilized in human medicine

48 and animal husbandry due to their broad-spectrum antimicrobial activity[1-2]. TC, one of

49 the most commonly used antibiotic, is extensively present in various environment owing

50 to its high water solubility and resistance to conventional degradation processes. Its

51 pervasive occurrence poses considerable risks to ecosystem sustainability and human

52 health, which is becoming increasingly urgent for effective governance strategies.

53 Conventional treatment techniques often suffer from operational complexity and the

54 potential for secondary environmental pollution, limiting their practical applicability[3-

55 4]. In response to these challenges, piezo-photocatalysis has emerged as an innovative

56 and integrated advanced oxidation process, demonstrating remarkable potential for the

57 effective decomposition of TC [5-7]. This hybrid approach ingeniously couples

58 photocatalytic with piezocatalytic processes, leveraging the piezophototronic effect to

59 facilitate the spatial separation of photogenerated electron-hole pairs via a built-in

60 polarization electric field. Such synergy not only suppresses charge carrier recombination

61 but also enhances overall catalytic activity, creating a mutually reinforcing mechanism.
62 For example, Gong et al. [8] developed an innovative BaTiO₃/TCN piezoelectric
63 photocatalyst, achieving a 91.0% degradation rate within 60 minutes under visible light
64 and ultrasonic vibration. Similarly, Wang et al. [9] constructed an α -Fe₂O₃/Bi₂WO₆ Z-
65 scheme heterojunction, which exhibited an exceptional TC degradation efficiency of 82%
66 within 20 minutes. The piezophototronic effect has been demonstrated to substantially
67 improve the separation efficiency of photogenerated charge carriers through the strong
68 driving force induced by the built-in polarization electric field [10-12]. This synergy
69 creates a positive feedback loop: the electron-hole pairs from photocatalysis enhance the
70 material's piezoelectric response[13-15]. Consequently, piezo-photocatalysis represents a
71 pioneering and sustainable strategy for environmental antibiotic remediation.

72 Significant efforts have been devoted to designing piezo-photocatalytic
73 heterostructures for enhanced catalytic performance. For example, Fu et al. [16]
74 synthesized BaTiO₃/TiO₂ core-shell nanofibers, which demonstrated excellent piezo-
75 photocatalytic activity in organic pollutant degradation. Wu et al. [17] developed an S-
76 scheme V-BiOIO₃/FTCN heterojunction system that achieved remarkable tetracycline
77 (TC) removal efficiency through synergistic piezo-photocatalysis. Additionally, the
78 BiOBr/BaTiO₃ heterojunction showed dramatically enhanced activity under

79 simultaneous ultrasonication and light, with a rate constant of $20.839 \times 10^{-2} \text{ min}^{-1}$, far
80 exceeding piezo- or photocatalysis alone [18]. Despite these advances, conventional
81 heterostructures often suffer from complicated fabrication, interfacial instability, and
82 severe charge recombination at junction interfaces, which considerably limit their
83 practical applicability [7,19-20]. To overcome these limitations, researchers have focused
84 on developing single-component materials that intrinsically combine both piezoelectric
85 and photocatalytic properties. Such materials must simultaneously satisfy two critical
86 requirements: a high piezoelectric voltage coefficient and an appropriate bandgap
87 structure for visible-light absorption. Recent studies have identified several promising
88 semiconductor candidates, including ZnO, CdS, BiVO₄, and BaTiO₃, which demonstrate
89 effective degradation of hazardous pollutants under combined light irradiation and
90 mechanical stimulation [5,19-23]. Among these, monoclinic BiVO₄, with its suitable
91 bandgap (2.4 eV), has emerged as one of the most promising materials in the field of
92 piezo-photocatalysis due to its excellent visible light response, abundant surface oxygen
93 vacancies, and superior electronic conductivity [6, 22, 24]. Furthermore, the
94 polycrystalline phase structure and surface activity of BiVO₄ make it highly suitable for
95 coupling with other materials, thereby further enhancing the separation efficiency of
96 electron-hole pairs and improving catalytic performance [25-26].

97 Recently, noble metal nanoparticles (NPs) featuring the localized surface plasmon
98 resonance (LSPR) effect have garnered substantial attention as high-performance
99 catalytic materials[27-29]. The Fermi levels in noble metals can facilitate electron transfer
100 and extend the lifespan of charge carriers, thereby further enhancing catalytic activity [30-
101 31]. Bimetallic alloys, in particular, often demonstrate superior catalytic activity and
102 stability compared to their monometallic analogues due to synergistic electronic effects
103 [32-34]. For example, Jessi et al. [35] designed Pd/Au core - shell nanorodes that were
104 50 times more active than monometallic counterparts. Guan et al. [36] reported that a
105 bimetallic Pt-Au catalyst achieved 99% selectivity for haloanilines under mild conditions.
106 As typical noble metals, Pd and Pt nanoparticles are extensively applied in plasmonic
107 catalysis owing to their excellent chemical stability and reusability. Furthermore, Pt and
108 Pd are exceptional co-catalysts for the oxygen reduction reaction, which is a pivotal step
109 in the generation of superoxide radical anions. In the context of piezo-photocatalysis,
110 noble metals would also effectively trap piezo-induced electrons, creating a synergistic
111 ‘electron pool’ that maximizes the utilization of both photo and mechanical energy[37-
112 41]. The combination of a piezo-photocatalytic semiconductor like BiVO₄ with bimetallic
113 Pt-Pd NPs presents a compelling strategy to create a high-performance hybrid system.
114 This architecture can leverage the LSPR effect to enhance light absorption and create

115 efficient electron-sink sites, while the piezoelectric field from BiVO₄ further drives
116 charge separation. Although considerable efforts have been dedicated to exploring the
117 photocatalytic performance of BiVO₄ in environmental remediation, the application of
118 Pt-Pd/BiVO₄ piezo-photocatalysis for antibiotic degradation remains largely unexplored.

119 The catalytic mechanism in such a coupled system, where piezoelectricity,
120 photoexcitation, and LSPR effects interact, is fundamentally distinct from conventional
121 photocatalysis and requires dedicated investigation.

122 Herein, we report the preparation, characterization, and catalytic activity of Pt-
123 Pd/BiVO₄ piezo-photocatalyst for the degradation of antibiotics under visible light and/or
124 ultrasound. The decoration of BiVO₄ nanosheets with bimetallic Pt-Pd NPs modifies its
125 band structure and electronic distribution, thereby enhancing the stability and durability
126 of the heterostructure. Moreover, the synergistic effect among the bimetallic alloy,
127 localized surface plasmon resonance (LSPR), and piezo- photocatalysis effectively
128 suppresses the recombination of charge carriers and accelerates the kinetic process of the
129 catalytic reaction. The impacts of the Pt-Pd loading content, microtopography, and
130 surface chemical composition of the heterostructures on the piezo-photocatalytic
131 degradation of antibiotics are analyzed in detail. The mechanism underlying the enhanced
132 piezo-photocatalytic activity is elaborated through active species trapping and electron

133 spin resonance (ESR) tests. This study offers a novel approach for the design and
134 synthesis of semiconductor composites by introducing bimetallic NPs into piezo-
135 photocatalysts, holding great potential for applications in energy conversion and
136 environmental remediation.

137 **2. Experimental section**

138 *2.1 Materials*

139 All chemicals employed in this study were of analytical grade and obtained from
140 certified suppliers. The following reagents were procured from Sigma-Aldrich: bismuth
141 nitrate pentahydrate ($\text{Bi}(\text{NO}_3)_3 \cdot 5\text{H}_2\text{O}$, $\geq 98\%$), ammonium metavanadate (NH_4VO_3 ,
142 $\geq 99\%$), nitric acid (HNO_3 , 68–70%), aqueous ammonia ($\text{NH}_3 \cdot \text{H}_2\text{O}$, 28–30%), palladium
143 chloride (PdCl_2 , $\geq 99.9\%$), platinic chloride (PtCl_4 , $\geq 99.9\%$), sodium borohydride (NaBH_4 ,
144 $\geq 98\%$), and polyvinyl alcohol (PVA, $\text{Mw} \sim 31,000\text{--}50,000$). Tetracycline hydrochloride
145 (TC , $\geq 95\%$), 1,4-benzoquinone (BQ, $\geq 98\%$), tert-butyl alcohol (t-BuOH , $\geq 99.5\%$),
146 ethylenediaminetetraacetic acid disodium salt (EDTA-2Na, $\geq 99\%$), 5,5-dimethyl-1-
147 pyrroline-N-oxide (DMPO, $\geq 97\%$), and dimethyl sulfoxide (DMSO, $\geq 99.9\%$) were
148 purchased from Shanghai Aladdin Biochemical Technology Co., Ltd. All solutions were
149 prepared using ultrapure water ($18.2 \text{ M}\Omega \cdot \text{cm}$ at 25°C) obtained from a Millipore Milli-Q

150 water purification system to ensure experimental consistency and minimize interference
151 from impurities.

152 *2.2. Preparation of catalysts*

153 *2.2.1 Preparation of BiVO₄*

154 The monoclinic BiVO₄ was synthesized using a facile hydrothermal method, as
155 described in previous literature [42-43]. In a typical synthesis, 7.2 mmol of NH₄VO₃ and
156 7.2 mmol of Bi(NO₃)₃·5H₂O were initially dispersed in 80 mL of 2 mol L⁻¹ HNO₃
157 solution under continuous stirring. Following this, an aqueous ammonia solution was
158 gradually added to the mixture until a pH of 2.0 was achieved. The resulting yellow
159 suspension was then transferred into a Teflon-lined autoclave and subjected to
160 hydrothermal treatment at 180 °C for 24 hours. After the reaction, the yellow product was
161 collected via centrifugation, thoroughly washed with deionized water multiple times, and
162 dried at 80 °C overnight for subsequent use.

163 *2.2.2 Preparation of Pt-Pd/BiVO₄ heterojunction*

164 In this procedure, Pt-Pd noble alloy nanoparticles (NPs) were deposited onto the surface
165 of BiVO₄ via a reduction method. Aqueous solutions of the metal precursors, PdCl₂ (0.01
166 M) and PtCl₄ (0.01 M), were dispersed into a BiVO₄/PVA suspension under vigorous
167 stirring. A freshly prepared NaBH₄ solution (with a molar ratio of NaBH₄ to total metal
9

168 ions of 5:1) was promptly added to the mixture. The reaction was allowed to proceed
169 under continuous stirring for 24 hours in an ice bath. Subsequently, the product was
170 collected and washed multiple times with deionized water and ethanol. The as-
171 synthesized samples were then dried in a vacuum oven for further characterization and
172 use. For comparative analysis, Pt-Pd/BiVO₄ heterojunctions with varying loading
173 percentages of Pt and Pd were prepared and labeled as PPB-0.1, PPB-0.3, PPB-0.5, and
174 PPB-0.7, respectively. Additionally, Pt/BiVO₄ and Pd/BiVO₄ samples were synthesized
175 following the same procedure for reference. Actual Pt and Pd loadings in the BiVO₄
176 nanosheets, as measured by ICP-OES, are summarized in **Table 1**.

177 *2.3 Catalyst characterization*

178 The morphology and structure of as-prepared samples were obtained by
179 transmission electron microscopy (TEM; JEM-2100F, JEOL Ltd). The crystal structure
180 was characterized by X-ray diffraction patterns (XRD, D2 PHASER, Bruker) with Cu K α
181 as radiation (30 kV, $\lambda = 1.542 \text{ \AA}$) in a range of 10–70° (2 θ). Fourier transform infrared
182 (FTIR) spectra was recorded in a Bruker infrared spectrometer (VERTEX 80V, Germany).
183 The chemical states and elemental compositions of the as-synthesized samples were
184 observed by X-ray photoelectron spectroscopy (XPS, ESCA LAB MK-II) with
185 monochromatized Al K α radiation, using an ion source energy for charge compensation.

186 Ultraviolet-visible diffuse reflectance spectra (UV-vis DRS) were performed by a Hitachi
187 S-3100 spectrophotometer. An N₂ adsorption-desorption analyzer (BEL BELSORP) was
188 employed to measure the specific surface area, pore size, and pore volume of the catalysts.
189 The active species in the degradation process were detected by trapping experiments.
190 Radical scavengers, including benzoquinone (BQ), *t*-butanol (*t*-BuOH), and disodium
191 ethylenediaminetetraacetate (EDTA-2Na), were introduced into the catalytic system to
192 capture superoxide radicals (·O²⁻), hydroxyl radicals (·OH), and holes (h⁺), respectively.
193 The electron spin resonance (ESR) measurements were detected by using 5,5-dimethyl-
194 1-pyrroline-N-oxide (DMPO) as spin-trapping agent on a Bruker EMX PLUS
195 spectrometer.

196 *2.4 Photoelectrochemical and piezophotoelectrochemical activity*
197 The photoelectrochemical (PEC) measurements were conducted using an Ivium
198 electrochemical workstation equipped with a standard three-electrode system. A platinum
199 wire served as the counter electrode, an Ag/AgCl electrode as the reference electrode, and
200 0.2 M aqueous Na₂SO₄ solution as the electrolyte. To evaluate the
201 piezophotoelectrochemical activity, the three-electrode cell assembly was placed in an
202 ultrasonic transducer with a power of ~100 W and a frequency of ~40 kHz. A 300 W
203 xenon lamp was utilized as the light source for the PEC measurements. Both photocurrent

204 response and electrochemical impedance spectroscopy (EIS) analyses were performed
205 using the electrochemical workstation with the three-electrode configuration.

206 *2.5 Piezo-photocatalytic TC measurement*

207 The piezo-photocatalytic performance of the PPB catalysts was evaluated through
208 the degradation of tetracycline (TC). In a typical experiment, 10 mg of the catalyst was
209 dispersed into 100 mL of an aqueous TC solution (20 mg/L). Before initiating the reaction,
210 the suspension was stirred in the dark for 30 minutes to achieve adsorption-desorption
211 equilibrium between the catalyst and the TC solution. The degradation experiment was
212 conducted under light irradiation (using a 300 W Xe lamp with a 350 nm bandpass filter,
213 100 mW/cm²) and/or ultrasonic treatment (100 W, 40 kHz). At specified time intervals,
214 5.0 mL of the reaction solution was collected, centrifuged, and analyzed using a UV
215 spectrophotometer to monitor the degradation progress. Additionally, electron spin
216 resonance (ESR) measurements were performed to detect reactive species. These
217 measurements utilized 5,5-dimethyl-1-pyrroline-N-oxide (DMPO) as a spin-trapping
218 agent and were carried out on a Bruker EMX PLUS spectrometer.

219 For quantitative evaluation, the degradation rate and kinetics were applied to
220 describe the degradation effect, the following Eq. (1) and (2)

221
$$\text{Degradation efficiency} = (C_0 - C_t / C_0) \times 100\% \quad (1)$$

222 $kt = -\ln(C_t/C_0)$ (2)

223 where C_0 and C_t are the initial and residual concentration of TC; k is the rate constant,
224 and t is the reaction time.

225 **3. Results and discussion**

226 *3.1. Crystal stucture and composition*

227 The Pt-Pd/BiVO₄ composite was synthesized via a combination of hydrothermal and
228 chemical reduction methods, with varying concentrations of Pt-Pd. The crystallographic
229 structures of the as-prepared catalysts were characterized using XRD analysis, as depicted
230 in **Fig. 1a**. The diffraction peaks corresponding to BiVO₄ matched well with the
231 monoclinic structure of BiVO₄ (JCPDS card No. 14-0688) [44-45]. As the weight ratio of
232 Pt-Pd nanoparticles (NPs) increased, the characteristic peaks of BiVO₄ slightly weakened,
233 indicating the successful formation of Pt-Pd/BiVO₄ composites. No diffraction peaks of
234 Pd or Pt species were observed, which is consistent with the formation of a highly
235 dispersed bimetallic structure. The absence of separate metallic peaks, combined with the
236 HR-TEM evidence, further supports the formation of highly dispersed bimetallic entities
237 rather than large, segregated crystalline phases(**Fig. S1**).In the FT-IR spectra (**Fig. S2**),
238 the two characteristic peaks at 758 and 852 cm⁻¹ were attributed to the asymmetrical and
239 symmetrical stretching vibrations of the VO₄³⁻ tetrahedron in BiVO₄ [45-46]. No distinct

240 diffraction peaks associated with Pt or Pd species were observed, likely due to their low
241 concentration and high dispersion on the BiVO₄ surface. Raman spectroscopy was further
242 employed to analyze the structure of the as-prepared materials (**Fig. 1b**). The Raman
243 spectra of pristine BiVO₄ exhibited peaks at 125, 210, 327, 366, 710, and 828 cm⁻¹,
244 corresponding to the external mode (rotation/translation), symmetric/asymmetric bending
245 modes, and asymmetric/symmetric V-O stretching modes, respectively. Notably, the
246 higher intensity vibrational bands observed for PPB-0.5 were likely due to the surface-
247 enhanced Raman scattering (SERS) effect induced by the Pt/Pd NPs, suggesting a strong
248 interaction between Pt-Pd and BiVO₄. To further confirm the presence of Pt and Pd, the
249 samples were analyzed using TEM and XPS techniques. These analyses provided
250 additional evidence for the successful incorporation and dispersion of Pt-Pd NPs on the
251 BiVO₄ surface.

252 The morphologies of the synthesized PPB-0.5 catalysts were characterized using
253 TEM, as illustrated in **Fig. 2**. From **Fig. 2a** and 2b, it is evident that bimetallic Pt-Pd
254 nanoparticles (NPs) with sizes ranging from 5 to 10 nm were uniformly dispersed on the
255 surface of the BiVO₄ nanosheets. High-resolution TEM analysis revealed well-defined
256 lattice fringes measuring 0.253 nm, which can be indexed to the (002) planes of
257 crystalline BiVO₄. Lattice fringes with interplanar spacings of 0.226 nm and 0.224 nm

258 were clearly observed in **Fig. S1**, which corresponded to the crystal plane of Pt and crystal
259 plane of Pd, respectively. This uniform dispersion is critical for facilitating efficient
260 charge transfer. Energy-dispersive X-ray (EDX) spectroscopy mapping images (**Fig. 2c-**
261 **h**) further confirmed the homogeneous distribution of Pd, Pt, Bi, V, and O elements,
262 providing strong evidence for the successful integration of Pt-Pd NPs with BiVO₄ in the
263 composite. To assess the piezoelectric properties of the Pt-Pd/BiVO₄ catalysts,
264 piezoelectric force microscopy (PFM) was employed. The topography, amplitude, and
265 phase images of PPB-0.5 (**Fig. 3a-c**) revealed a distinct piezopotential and clear phase
266 differences, indicating significant piezoelectric behavior. The corresponding amplitude
267 loop exhibited a characteristic butterfly shape, with a maximum amplitude of
268 approximately 600 pm under ± 10 V ramp voltage loop (**Fig. 3e**). Additionally, a well-
269 defined 180° phase angle inversion was observed (**Fig. 3d**), further confirming the
270 presence of a local piezoelectric field in the PPB-0.5 catalyst. These results collectively
271 demonstrate the enhanced piezoelectric properties of the PPB-0.5 composite.

272 The specific surface area and pore characteristic of Pt-Pd/BiVO₄ composites were
273 estimated by N₂ sorption analysis (**Fig. 4**). As shown in **Table S1**, the SBET of the BiVO₄,
274 Pd/BiVO₄, and PPB-0.5 is calculated as 4.4 m²/g, 7.1 m²/g, and 10.5 m²/g (type IV),
275 respectively. Compared to pure BiVO₄, the PPB-0.5 composite possesses a significantly

276 higher specific surface area. We attribute this to the dual function of the metal precursors,
277 which act as a growth moderator during BiVO_4 crystallization. This process inhibits
278 excessive crystallite growth and agglomeration, resulting in a finer and more porous
279 microstructure, thereby imparting a higher specific surface area (**Fig. 4a**). The pore size
280 distribution curves (**Fig. 4b**) revealed that a wide range of macropores (2-40 nm),
281 according to the IUPAC definition. The well-developed pore structures and higher
282 specific surface areas are beneficial to enhancing the catalytic performance through
283 facilitating reactant adsorption and charge conduction[47-48]. As a result, the
284 introduction of bimetallic Pt-Pd NPs is expected to effectively degrade pollutants in the
285 degradation process.

286 The surface compositions and chemical states of the catalysts were analyzed using
287 XPS. The full-scan survey spectra (**Fig. 5a**) of the as-prepared samples revealed distinct
288 XPS signals corresponding to Bi, V, O, Pt, and Pd, consistent with the elemental mapping
289 results (**Fig. 2**). As shown in **Fig. 5b**, the two spin-orbit splitting peaks at 163.9 eV and
290 169.2 eV were assigned to the Bi $4f_{7/2}$ and Bi $4f_{5/2}$ states of Bi^{3+} species, respectively. In
291 the V $2p_{3/2}$ XPS spectra (**Fig. 5c**), the two peaks at 521.2 eV and 516.4 eV were associated
292 with the surface V species in the PPB-0.5 phase. The O 1s spectrum (**Fig. 5d**) exhibited
293 two characteristic peak at 533.7 and 529.8 eV, corresponding to the oxygen species and

294 hydroxyl groups in PPB-0.5. As illustrated in **Fig. 5e**, three distinct platinum species are
295 identified based on their characteristic binding energies: Pt⁴⁺ (74.9 eV), Pt²⁺ (72.6 eV),
296 and Pt⁰ (71.2 eV). For the Pd 3d spectrum (**Fig. 5f**), four peaks were observed at 341.5
297 eV, 339.5 eV, 336.2 eV, and 334.5 eV, which were attributed to Pd 3d_{3/2}(Pd²⁺), Pd
298 3d_{3/2}(Pd⁰), Pd 3d_{5/2}(Pd²⁺), and Pd 3d_{5/2} (Pd⁰), respectively. Additionally, the presence of
299 zero oxidation states for both metallic Pd and Pt NPs (**Fig. 5e** and **5f**) confirmed the
300 successful deposition of Pd and Pt NPs on the surface of the photocatalysts. Generally,
301 variations in electron density can lead to shifts in binding energies due to electron
302 screening effects. The observed shift in binding energies toward higher values upon
303 combining Pt and Pd NPs with BiVO₄ (**Fig. 5**) further corroborates the formation of the
304 PPB-0.5 hybrid structure.

305 *3.2. Optical and electronic characteristics*

306 The UV-vis diffuse reflectance spectroscopy (DRS) (**Fig. 6a**) was employed to
307 evaluate the light absorption properties of the samples. The absorption edge of pure
308 BiVO₄ was observed at approximately 550 nm, corresponding to the band transition from
309 the Bi 6s orbital to the V 3d conduction band. The Pt-Pd/BiVO₄ composite exhibited
310 enhanced light absorption with a slight red shift in the visible light region, indicating
311 improved visible light utilization. This enhancement can be attributed to the deposition

312 of metallic Pt and Pd species on the crystal facets of BiVO₄, which induced a surface
313 plasmon resonance (SPR) effect. The as-prepared BiVO₄ exhibits a bandgap energy of
314 ~2.4 eV, determined from the extrapolated intercept on the abscissa.

315 To investigate the generation, transfer, and separation of charge carriers during the
316 catalytic reaction, transient photocurrent measurements were conducted under
317 simultaneous light irradiation and ultrasound. As shown in **Fig. 6b**, the PPB-0.5 sample
318 demonstrated the highest photocurrent density among all samples, consistent with its
319 superior piezo-photocatalytic performance. To further explore the influence of the
320 piezoelectric field on photocatalysis, the photocurrent response of PPB-0.5 was measured
321 with and without ultrasound (**Fig. 6c**). Notably, the photocurrent density significantly
322 increased when ultrasound was applied, demonstrating that the piezoelectric field
323 generated by vibrational energy effectively promoted the separation and migration of
324 photogenerated charge carriers, thereby enhancing the photocurrent response.

325 Electrochemical impedance spectroscopy (EIS) measurements were conducted to
326 further assess the charge transfer behavior of the as-prepared samples. As shown in **Fig.**
327 **6d**, the EIS Nyquist plots revealed that the PPB-0.5 composite exhibited the smallest
328 radius of the impedance arc among all samples. This indicates that the PPB-0.5 composite
329 facilitated more efficient charge carrier separation and transfer, thereby enhancing the
18

330 oxidation reaction kinetics. Moreover, the emission band observed at 490-510 nm (**Fig.**
331 **S3**) corresponds to the band-band photoluminescence (PL) phenomenon characteristic of
332 BiVO_4 . Notably, Pt-Pd/ BiVO_4 exhibits significant PL emission quenching compared to
333 pristine BiVO_4 , demonstrating that the built-in potential effectively suppresses charge
334 recombination. The PL intensity was further decreased upon ultrasound application,
335 clearly indicating that the piezoelectric field effectively facilitated the separation and
336 migration of photogenerated charge carriers.

337 *3.3. Piezo-photocatalytic degradation of TC*

338 The catalytic performance of the as-prepared samples was evaluated by monitoring
339 the variation in tetracycline (TC) concentration over time under different conditions (i.e.,
340 light irradiation, ultrasound, and combined light irradiation with ultrasound). Compared
341 to individual piezocatalysis and photocatalysis, the piezo-photocatalysis system
342 demonstrated significantly enhanced degradation activity. Among all the catalysts, PPB-
343 0.5 exhibited the highest catalytic efficiency for TC degradation (**Fig. 7a, c, e**). Notably,
344 99.9% of TC was degraded over PPB-0.5 under simultaneous ultrasonic vibration and
345 visible light irradiation within 50 minutes, while the degradation efficiency for pure
346 BiVO_4 was only 65.4%. This remarkable improvement can be attributed to the synergistic
347 effects of surface plasmon resonance (SPR), photocatalysis, and piezoelectric properties

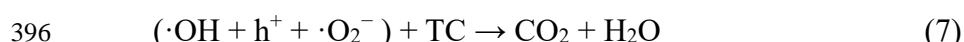
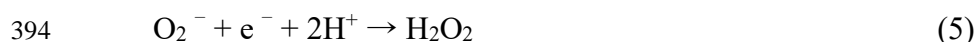
348 resulting from the loading of Pt and Pd nanoparticles (NPs) on the BiVO₄ surface. The
349 corresponding pseudo-first-order reaction kinetics for TC degradation are presented in
350 **Fig. 7b, d, f.** The high reaction rate constant (K) of Pt-Pd/BiVO₄ under photocatalysis,
351 piezocatalysis, and piezo-photocatalysis further confirmed its superior degradation
352 efficiency. These results highlight that the enhanced catalytic performance is primarily
353 due to the formation of intimate interfaces between Pt-Pd NPs and BiVO₄, which establish
354 a continuous pathway for charge migration. Additionally, the composite maintained
355 approximately 89% of its initial activity after four consecutive cycles (Fig. 8a),
356 demonstrating a reasonable degree of operational stability. The XRD and XPS patterns of
357 PPB-0.5 before and after use (**Figs. S4 and S5**) remained nearly identical, confirming its
358 structural stability and reusability. The efficiency decline is likely attributed to the
359 progressive coverage of active sites by strongly adsorbed organic intermediates generated
360 during the incomplete mineralization of TC. A comparison of the piezo-photocatalytic
361 performance of PPB-0.5 with various catalysts reported in the literature is summarized in
362 **Table 2**[49-54]. The results indicate that the PPB-0.5 composite exhibits superior TC
363 degradation efficiency compared to most other catalytic systems, underscoring its
364 potential for practical applications in pollutant degradation.

365 *3.4. Mechanism study*

366 To identify the active species generated during the piezo-enhanced photocatalytic
367 reaction, trapping experiments were conducted using PPB-0.5.
368 Ethylenediaminetetraacetic acid (EDTA), tert-butanol (t-BuOH), and benzoquinone (BQ)
369 were employed as scavengers to trap h^+ , $\cdot OH$, and $\cdot O_2^-$ species, respectively. The time-
370 dependent piezo-photocatalytic degradation curves of TC are shown in **Fig. 8b**, revealing
371 that the addition of scavengers suppressed the TC degradation efficiency to varying
372 degrees. Notably, the introduction of BQ, as a $\cdot O_2^-$ quencher, had the most significant
373 inhibitory effect, indicating that $\cdot O_2^-$ played a dominant role in the TC degradation
374 process. To further validate the catalytic mechanism, electron spin resonance (ESR)
375 measurements were performed. As illustrated in **Fig. S6** and **Fig. 8c-d**, characteristic
376 signals corresponding to DMPO- $\cdot OH$ and DMPO- $\cdot O_2^-$ were detected for BiVO₄,
377 Pt/BiVO₄, Pd/BiVO₄, and PPB-0.5, confirming the generation of reactive species. No
378 radical signals were observed under dark conditions. When only ultrasonic vibration was
379 applied, weak radical signals emerged, suggesting a limited piezocatalytic effect.
380 However, under light irradiation, a significant enhancement in radical signal intensity was
381 observed, highlighting the dominant role of photocatalytic activity in radical generation.
382 Importantly, the signal intensities of $\cdot OH$ and $\cdot O_2^-$ for PPB-0.5 were the strongest among
383 all samples under combined vibration and light irradiation, demonstrating that more

384 reactive radicals ($\cdot\text{OH}$ and $\cdot\text{O}_2^-$) were generated during the piezo-photocatalytic reaction.
385 These results indicate that the PPB-0.5 piezo-photocatalysis system efficiently generates
386 more photogenerated charge carriers, which participate in redox reactions through the
387 built-in polarization field, thereby enhancing the overall catalytic performance. The
388 identified radical-based mechanism ($\cdot\text{OH}$ and $\cdot\text{O}_2^-$), known for its non-selective oxidation
389 of diverse organic compounds, indicates that PPB-0.5 holds inherent potential for broad-
390 spectrum environmental remediation, including the removal of dyes and pharmaceuticals.

391 The piezo-photocatalytic reaction mechanism can be summarized as follows:



397 Based on theoretical insights and the experimental results, a plausible mechanism
398 for the piezo-photocatalytic degradation of TC over Pt-Pd/BiVO₄ is proposed. As
399 illustrated schematically in **Fig. 9**, the hydrothermally synthesized BiVO₄ nanosheets are
400 considered as a moderate bandgap semiconductor, possessing a bandgap of ≈ 2.4 eV.

401 Under visible light irradiation, PPB-0.5 is excited to generate electron-hole pairs. The

402 photogenerated electrons in the conduction band (CB) of BiVO₄ rapidly migrate to the
403 surface of Pt-Pd nanoparticles (NPs), while the photogenerated holes remain in the
404 valence band (VB). Simultaneously, mechanical stress induces the formation of polarized
405 electric fields in BiVO₄, which accumulate positive and negative charges on opposite
406 crystal surfaces. The synergistic effects of piezoelectric polarization and the surface
407 plasmon resonance (SPR) effect facilitate the effective separation and rapid transfer of
408 photogenerated carriers to the catalyst surface, significantly reducing the recombination
409 rate of electron-hole pairs. During the degradation process, the accumulated electrons on
410 the surface activate TC to produce ·O₂⁻ radicals, while the photogenerated holes in the
411 VB react with OH⁻ in the solution to form ·OH radicals. By integrating the SPR effect,
412 photocatalytic activity, and piezoelectric properties, PPB-0.5 generates a higher
413 concentration of active radicals, which actively participate in the TC degradation reaction.
414 This synergistic mechanism results in significantly enhanced piezo-photocatalytic
415 performance, demonstrating the superior efficiency of the PPB-0.5 system in pollutant
416 degradation.

417 **Conclusions**

418 In this study, bimetallic Pt-Pd NP-decorated BiVO₄ piezo-photocatalysts (Pt-
419 Pd/BiVO₄) were successfully synthesized using a facile hydrothermal and chemical

420 reduction method. The prepared PPB-0.5 composites exhibited significantly enhanced
421 piezo-photocatalytic activity for TC degradation compared to pure BiVO₄. This improved
422 performance is primarily attributed to the synergistic effects of the surface plasmon
423 resonance (SPR) effect, photocatalytic activity, and piezoelectric properties, which
424 collectively enhance carrier transport efficiency. Notably, the PPB-0.5 heterojunction
425 demonstrated the highest piezo-photocatalytic performance, achieving nearly complete
426 degradation (99.9%) of TC in wastewater within 50 minutes. Furthermore, the PPB-0.5
427 catalysts maintained excellent stability, with only a minimal loss of activity after four
428 consecutive cycles. While the noble metal cost challenges scale-up, the high performance
429 and stability of PPB-0.5 provide a compelling proof-of-concept. This work provides new
430 insights into the design of highly efficient piezo-photocatalysts for pollutant degradation,
431 highlighting the significant contributions of the SPR effect and piezoelectric properties to
432 the photocatalytic activity of piezoelectric materials. These findings pave the way for the
433 development of advanced catalytic systems for environmental remediation.

434

435 CRediT authorship contribution statement

436 **Hao Sun:** Writing-original draft, Methodology, Formal analysis, Data curation,

437 **Xu Zhao:** Supervision, Resources, Funding acquisition, Methodology,

438 Writing-review & editing. **Martin R. Tillotson**: Writing-review & editing, Methodology,

439 Investigation. **Wei Guo**: Writing-review & editing, Validation, Conceptualization.

440

441 **Acknowledgements**

442 This work was supported by the National Natural Science Foundation of China

443 (72074136 and 72033005); Major Grant in National Social Sciences of China

444 (23VRC037, 24VHQ018); Shandong Provincial Natural Science Foundation

445 (ZR2024MG008); the Taishan Scholar Youth Expert Program of Shandong Province (NO.

446 tsqn202103020); the National Key Research and Development Program of China

447 (2022YFC3105304).

448 **Data availability**

449 Data will be made available on request.

450

451

452

453

454

455

456

457

458

459

460

461 [1] W. Witte, Medical consequences of antibiotic use in agriculture. *Science*. 279 (1998)

462 996-997.

463 [2] B.M. Marshall, S.B. Levy, Food animals and antimicrobials: impacts on human health.

464 *Clin Microbiol rev.* 24 (2011) 718-733.

465 [3] H. Shi, C. Wang, Y. Zhao, E. Liu, J. Fan, Z. Ji, Highly efficient visible light driven

466 photocatalytic inactivation of *E. coli* with Ag QDs decorated Z-scheme $\text{Bi}_2\text{S}_3/\text{SnIn}_4\text{S}_8$

467 composite, *Appl Catal B.* 254 (2019) 403-413.

468 [4] P. Rokicka-Konieczna, A. Markowska-Szczupak, E. Kusiak-Nejman, A. W. Morawski,

469 Photocatalytic water disinfection under the artificial solar light by fructose-modified TiO_2 ,

470 *Chem. Eng. J.* 372 (2019) 203-215.

471 [5] L. Jing, Y. Xu, M. Xie, Z. Li, C. Wu, H. Zhao, J. Wang, H. Wang, Y. Yan, N. Zhong,

472 H. Li, J. Hu, Piezo-photocatalysts in the field of energy and environment: Designs,
473 applications, and prospects. *Nano Energy.* 112 (2023) 108508.

474 [6] P. Jia, J. Li, H. Huang. Piezocatalysts and Piezo-Photocatalysts: From Material Design
475 to Diverse Applications. *Adv Funct Mater.* 34 (2024) 2407309.

476 [7] H. Zheng, Y. Wang, J. Liu, J. Wang, K. Yan, K. Zhu, Recent advancements in the use
477 of novel piezoelectric materials for piezocatalytic and piezo-photocatalytic applications.
478 *Appl. Catal. B-Environ. Energy.* 341 (2024) 123335.

479 [8] S. Gong, W. Zhang, Z. Liang, Y. Zhang, T. Gan, H. Hu, Z. Huang, Construction of a
480 BaTiO₃/tubular g-C₃N₄ dual piezoelectric photocatalyst with enhanced carrier separation
481 for efficient degradation of tetracycline. *Chem Eng J.* 461 (2023) 141947.

482 [9] X. Zhang, C. Hu, Z. Zhu, Y. Zhang, S. Tu, Y. Zhang, H.
483 Huang, T. Ma, F. Chen, Efficient piezo-photocatalysis of 0D/2D α -Fe₂O₃/Bi₂WO₆:
484 Synergy of weak force-driven piezoelectric polarization and Z-scheme junction. *J Colloid
485 Interf Sci.* 650 (2023) 1536-1549.

486 [10] X. Huang, K. Wang, Y. Wang. B. Wang, L. Zhang, F. Guo, Y. Zhao, W. Feng, S.
487 Zhang, P. Liu, Enhanced charge carrier separation to improve hydrogen production
488 efficiency by ferroelectric spontaneous polarization electric field. *Appl. Catal. B.* 227
489 (2018) 322-329.

490 [11] B. Dai, G. Biesold, M. Zhang, H. Zou, Y. Ding, Z. Wang, Z. Lin, Piezo-phototronic
491 effect on photocatalysis, solar cells, photodetectors and light-emitting diodes. *Chem Soc*
492 *Rev.* 50 (2021) 13646-13691.

493 [12] D. You, L. Liu, Z. Yang, X. Xing, K. Li, W. Mai, T. Guo, G. Xiao, C. Xu,
494 Polarization-induced internal electric field to manipulate piezo-photocatalytic and ferro-
495 photoelectrochemical performance in bismuth ferrite nanofibers. *Nano Energy*. 93 (2022)
496 106852.

497 [13] J. Yuan, X. Huang, L. Zhang, F. Gao, R. Lei, C. Jiang, W. Feng, P. Liu, Tuning
498 piezoelectric field for optimizing the coupling effect of piezo-photocatalysis. *Appl. Catal.*
499 *B.* 278 (2020) 119291.

500 [14] X. Zhou, B. Shen, A. Lyubartsev, J. Zhai, N. Hedin, Semiconducting piezoelectric
501 heterostructures for piezo-and piezophotocatalysis. *Nano Energy*. 96 (2022) 107141.

502 [15] Q. Zhu, K. Zhang, D. Li, N. Li, J. Xu, D. Bahnemann, C. Wang, Polarization-
503 enhanced photocatalytic activity in non-centrosymmetric materials based photocatalysis:
504 A review. *Chem Eng J.* 426 (2021) 131681.

505 [16] B. Fu, J. Li, H. Jiang, X. He, Y. Ma, J. Wang, C. Hu, Modulation of electric dipoles
506 inside electrospun $\text{BaTiO}_3@\text{TiO}_2$ core-shell nanofibers for enhanced piezo-photocatalytic
507 degradation of organic pollutants. *Nano Energy*. 93 (2022) 106841.

508 [17] T. Wu, Q. Liang, L. Tang, J. Tang, J. Wang, B. Shao, S. Gong, Q. He, Y. Pan, Z. Liu,
509 Construction of a novel S-scheme heterojunction piezoelectric photocatalyst V-
510 BiOIO₃/FTCN and immobilization with floatability for tetracycline degradation. J Hazard
511 Mater. 443 (2023) 130251.

512 [18] S. Zhong, Y. Wang, Y. Chen, X. Jiang, M. Lin, C. Lin, T. Lin, M. Gao, C. Zhao, X.
513 Wu, Improved piezo-photocatalysis for aquatic multi-pollutant removal via
514 BiOBr/BaTiO₃ heterojunction construction. Chem Eng J. 488 (2024) 151002.

515 [19] S. Tu, Y. Guo, Y. Zhang, C. Hu, T. Zhang, T. Ma, H. Huang, Piezocatalysis and
516 piezo-photocatalysis: catalysts classification and modification strategy, reaction
517 mechanism, and practical application. Adv Funct Mater. 30 (2020) 2005158.

518 [20] S.C. Panchangam, C.S. Yellatur, J.S. Yang, S.S. Loka, A.Y.C. Lin, V. Vemula, Facile
519 fabrication of TiO₂-graphene nanocomposites (TGNCs) for the efficient photocatalytic
520 oxidation of perfluorooctanoic acid (PFOA). J Environ Chem Eng. 6 (2018) 6359-6369.

521 [21] M. Zhang, S. Nie, T. Cheng, Y. Feng, C. Zhang, L. Zheng, L. Wu, W. Hao, Y. Ding,
522 Enhancing the macroscopic polarization of CdS for piezo-photocatalytic water splitting.
523 Nano Energy. 90 (2021) 106635.

524 [22] F. Wang, J. Zhang, C. Jin, X. Ke, F. Wang, D. Liu, Unveiling the effect of crystal
525 facets on piezo-photocatalytic activity of BiVO₄. Nano Energy. 101 (2022) 107573.

526 [23] Y. Jiang, C. Toe, S. Mofarah, C. Cazorla, S. Chang, Y. Yin, Q. Zhang, S. Lim, Y. Yao,
527 R. Tian, Y. Wang, T. Zaman, H. Arandiyan, G. Andersson, J. Scott, P. Koshy, D. Wang, C.
528 Sorrell, Efficient cocatalyst-free piezo-photocatalytic hydrogen evolution of defective
529 BaTiO_{3-x} nanoparticles from seawater. ACS Sustainable Chem Eng. 11 (2023) 3370-3389.

530 [24] Y. Cheng, T. Yu, X. Lei, B. Wang, W. Mu, X. Liu, R. Guo, Regulation of oxygen
531 vacancy by in-situ piezoelectric synthesized BiVO₄ to induce spin polarization for
532 boosting the piezo-photocatalytic activity. Chem. Eng. J. 504 (2024) 158900.

533 [25] C.N Van, W.S. Chang, J.W. Chen, K.A. Tsai, W.Y. Tzeng, Y.C. Lin, H.H. Kuo, H.J.
534 Liu, K.D. Chang, W.C. Chou, C.L. Wu, Y.C. Chen, C.W. Luo, Y.J. Hsu, Y.H. Chu,
535 Heteroepitaxial approach to explore charge dynamics across Au/BiVO₄ interface for
536 photoactivity enhancement. Nano Energy. 15 (2015) 625-633.

537 [26] A.J.E. Rettie, H.C. Lee, L.G. Marshall, J.F. Lin, C. Capan, J. Lindemuth, J.S. McCloy,
538 J.S. Zhou, A.J. Bard, C.B. Mullins, Combined charge carrier transport and
539 photoelectrochemical characterization of BiVO₄ single crystals: intrinsic behavior of a
540 complex metal oxide. J. Am. Chem. Soc. 135 (2013) 11389-11396.

541 [27] J. Zhao, S. Xue, R. Ji, B. Li, J. Li, Localized surface plasmon resonance for enhanced
542 electrocatalysis. Chem Soc Rev. 50 (2021) 12070-12097.

543 [28] A. Gelle, T. Jin, L. de la Garza, G.D. Price, L.V. Besteiro, A. Moores, Applications

544 of plasmon-enhanced nanocatalysis to organic transformations. *Chem. Rev.* 120 (2019)

545 986-1041.

546 [29] J. Yang, Y. Guo, W. Lu, R. Jiang, J. Wang, Emerging applications of plasmons in

547 driving CO₂ reduction and N₂ fixation. *Adv Mater.* 30 (2018) 1802227.

548 [30] M. Wang, M. Ye, J. Iocozzia, C. Lin, Z. Lin, Plasmon-mediated solar energy

549 conversion via photocatalysis in noble metal/semiconductor composites. *Adv Sci.* 3 (2016)

550 1600024.

551 [31] A. Zada, P. Muhammad, W. Ahmad, Z. Hussain, S. Ali, M. Khan, Q. Khan, M.

552 Maqbool, Surface plasmonic-assisted photocatalysis and optoelectronic devices with

553 noble metal nanocrystals: design, synthesis, and applications. *Adv Funct Mater.* 30. (2020)

554 1906744.

555 [32] A. Wang, X.Y. Liu, C.Y. Mou, T. Zhang, Understanding the synergistic effects of gold

556 bimetallic catalysts. *J catal.* 308 (2013) 258-271.

557 [33] X. Zhou, C. Luo, M. Luo, Q.L. Wang, J. Wang, Z.W. Liao, Z. Chen, Z. Chen,

558 Understanding the synergetic effect from foreign metals in bimetallic oxides for PMS

559 activation: A common strategy to increase the stoichiometric efficiency of oxidants. *Chem*

560 *Eng J.* 381 (2020) 122587.

561 [34] J. Fan, H. Du, Y. Zhao, Q. Wang, Y. Liu, D. Li, J. Feng, Recent progress on rational

562 design of bimetallic Pd based catalysts and their advanced catalysis. ACS Catal. 10 (2020)

563 13560-13583.

564 [35] J.E.S. van der Hoeven, J. Jelic, L.A. Olthof, G. Totarella, R.J.A. van Dijk-Moes, J.M.

565 Krafft, C. Louis, F. Studt, A. van Blaaderen, P.E. de Jongh, Unlocking synergy in

566 bimetallic catalysts by core-shell design. Nat mater. 20 (2021) 1216-1220.

567 [36] Q. Guan, C. Zhu, Y. Lin, E.I. Vovk, X. Zhou, Y. Yang, H. Yu, L. Cao, H. Wang, X.

568 Zhang, X. Liu, M. Zhang, S. Wei, W.X. Li, J. Lu, Bimetallic monolayer catalyst breaks

569 the activity-selectivity trade-off on metal particle size for efficient chemoselective

570 hydrogenations. Nat Catal. 4 (2021) 840-849.

571 [37] W. Ye, J. Yu, Y. Zhou, D. Gao, D. Wang, C. Wang, D. Xue, Green synthesis of Pt -

572 Au dendrimer-like nanoparticles supported on polydopamine-functionalized graphene

573 and their high performance toward 4-nitrophenol reduction. Appl. Catal. B. 181 (2016):

574 371-378.

575 [38] Y. Fan, A. Girad, M. Waals, C. Salzemann, A. Courty, Ag@Pt core-shell

576 nanoparticles for plasmonic catalysis. ACS Appl Nano Mater. 6 (2023) 1193-1202.

577 [39] H. Sun, S. Chen, W. Yang, L. Wang, R. Tang, X. Zhang, R. Zheng, S. Gu, Y. Jiang,

578 W. Liang, Plasmon-enhanced alcohol oxidations over porous carbon nanosphere-

579 supported palladium and gold bimetallic nanocatalyst. Appl. Catal. B. 292 (2021) 120151.

580 [40] C.S. Yellatur, R. Padmasale, S.S. Loka, Facile electrooxidation of ethanol on reduced
581 graphene oxide supported Pt-Pd bimetallic nanocomposite surfaces in acidic media.
582 Nanotechnology. 33.33 (2022) 335401.

583 [41] S. Challa, C.G.R. Nallagondu, R. Kulkarni, S.K. Godlaveeti, C.S. Yellatur, S.S. Loka,
584 N.S. Reddy, J.R. Koduru, A.R. Somala, Engineered Pt-Pd@ RGO-KI nanosheet catalyst
585 for enhanced electrocatalytic methanol oxidation performance. Mol Catal. 572 (2025)
586 114771.

587 [42] Y. Zhao, Y. Wang, H. Chi, Y. Zhang, C. Sun, H. Wei, R. Li, Coupling photocatalytic
588 water oxidation on decahedron BiVO₄ crystals with catalytic wet peroxide oxidation for
589 removing organic pollutions in wastewater. Appl. Catal. B. 318 (2022) 121858.

590 [43] Y. Wei, Y. Zhang, W. Geng, H. Su, M. Long, Efficient bifunctional piezocatalysis of
591 Au/BiVO₄ for simultaneous removal of 4-chlorophenol and Cr (VI) in water. Appl. Catal.
592 B. 259 (2019) 118084.

593 [44] H. Li, Y. Sun, B. Cai, S. Gan, D. Han, L. Niu, T. Wu, Hierarchically Z-scheme
594 photocatalyst of Ag@AgCl decorated on BiVO₄ (0 4 0) with enhancing
595 photoelectrochemical and photocatalytic performance. Appl. Catal. B. 170 (2015) 206-
596 214.

597 [45] K. Ji, H. Dai, J. Deng, H. Zang, H. Arandiyan, S. Xie, H. Yang, 3DOM BiVO₄

598 supported silver bromide and noble metals: High-performance photocatalysts for the
599 visible-light-driven degradation of 4-chlorophenol. *Appl. Catal. B.* 168 (2015) 274-282.

600 [46] B. Gao, Y. Pan, H. Yang, Enhanced photo-Fenton degradation of fluoroquinolones
601 in water assisted by a 3D composite sponge complexed with a S-scheme
602 $\text{MoS}_2/\text{Bi}_2\text{S}_3/\text{BiVO}_4$ ternary photocatalyst. *Appl. Catal. B.* 315 (2022) 121580.

603 [47] J. Wu, F. Xu, S. Li, P. Ma, X. Zhang, Q. Liu, R. Fu, D. Wu, Porous polymers as
604 multifunctional material platforms toward task - specific applications. *Adv Mater.* 31
605 (2019) 1802922.

606 [48] Y. Dong, J. Sun, Y. Shen, Z. Wang, W. Wang, Z. Song, X. Zhao, Y. Mao, 3D
607 snowflake graphene modified $\alpha\text{-MnO}_2$ Catalyst: Enhancing the Low-Temperature
608 catalytic activity for VOCs degradation. *Chem Eng J.* 473 (2023) 145130.

609 [49] C. Cheng, H. Tan, W. Zhu, L. Liu, K. Chen, J. Yan, The transition of tetragonal to
610 monoclinic phase in BiVO_4 coupled with peroxymonosulfate for photocatalytic
611 degradation of tetracycline hydrochloride. *Environ Res.* 267 (2025) 120631.

612 [50] P. Liu, D. Han, Z. Wang, F. Gu, Metal-organic framework CAU-17 derived Bi/BiVO_4
613 photocatalysts for the visible light-driven degradation of tetracycline hydrochloride. *Catal*
614 *Commun.* 177 (2023) 106657.

615 [51] F. Chen, Q. Yang, J. Sun, F. Yao, S. Wang, Y. Wang, X. Wang, C. Niu, D. Wang, G.

616 Zeng, Enhanced photocatalytic degradation of tetracycline by AgI/BiVO₄ heterojunction
617 under visible-light irradiation: mineralization efficiency and mechanism. ACS appl.
618 Mater. Interfaces. 8 (2016) 32887-32900.

619 [52] X. Fan, H. Liang, M. Zhang, C. Li, J. Bai, Bi/Bi₂S₃-BiVO₄ Z-scheme heterojunction
620 one-dimensional composites with efficient photocatalytic degradation of tetracycline:
621 Performance and mechanism insights. Colloid Surface A. 707 (2025)135929.

622 [53] Y. Cheng, Y. Zhang, C. Wang, T. Yu, X. Lei, R. Guo, Y. Tian, J. You, H. Zhang, X.
623 Wang, Enhancing the catalytic activity of BiVO₄: A new insight on the design of high-
624 efficiency piezo-photocatalyst. Colloid Surface A. 698 (2024) 134520.

625 [54] M. Lv, H. Wang, H. Shi, Construction of Z-scheme BiVO₄/NaNbO₃ piezo-
626 photocatalyst with improved carrier separation for efficient removal of tetracycline.
627 Colloid Surface A. 679 (2023) 132579.

628

629

630

631

632

633

634

635

636

637 **Fig. 1.** XRD spectra of BiVO₄ and Pt-Pd/BiVO₄ with different Pt-Pd loading contents;

638 (b) Raman spectra of the BiVO₄ and PPB-0.5 samples.

639 **Fig. 2.** (a-b) TEM of PPB-0.5 nanocomposites (c-h) elemental mapping patterns of PPB-

640 0.5 samples.

641 **Fig. 3.** (a) Topographic images, (b) amplitude images, (c) phase images, (d) amplitude-

642 voltage and (e) phase-voltage curves of PPB-0.5 samples.

643 **Fig. 4.** (a) Nitrogen adsorption-desorption isotherms of the synthesized samples; (b) pore

644 size distributions of the synthesized samples.

645 **Fig. 5.** XPS spectra of BiVO₄, Pt/BiVO₄, Pd/BiVO₄ and PPB-0.5 samples. (a) Survey

646 spectra; (b) Bi 4f; (c) V 2p; (d) O 1s (e) Pt 4f; (f) Pd 3d.

647 **Fig. 6.** (a) UV-vis DRS spectra of as-prepared samples; (b) Transient photocurrents of all

648 samples under light irradiation (L) and ultrasound (U); (c) Transient photocurrents of

649 PPB-0.5 in the presence or absence of ultrasound; (d) EIS of pBiVO₄, Pt/BiVO₄,

650 Pd/BiVO₄ and PPB-0.5 composites.

651 **Fig. 7.** (a) TC degradation experiments for BiVO₄, Pt/BiVO₄, Pd/BiVO₄ and Pt-Pd/BiVO₄

652 catalysts for (a) Piezocatalytic, (c) photocatalytic, and (e) piezo-photocatalytic
653 performance; and (b), (d) and (f) show the corresponding first-order kinetics plots of the
654 different catalysts.

655 **Fig. 8.** (a) Recycling runs of PPB-0.5; (b) photocatalytic performance of PPB-0.5 with
656 different species of quenchers (EDTA-2Na for h^+ , *t*-BuOH for $\cdot OH$, *P*-benzoquinone for
657 $\cdot O_2^-$); and (c-d) ESR spectra of BiVO₄, Pt/BiVO₄, Pd/BiVO₄ and PPB-0.5.

658 **Fig. 9.** Piezo-photocatalytic mechanism of TC degradation by PPB-0.5.